Int. J. Electrochem. Sci., 10 **(2015)** 5434 - 5455

International Journal of
ELECTROCHEMICAL
SCIENCE
www.electrochemsci.org

Corrosion- and Electrochemical Dissolution Behavior of Cast Iron Measured with Different Electrochemical Cell Types

Nicolas Zapp[1], *Olivier Weber*[2,3], *Harald Natter*[1,*]

[1] Physical Chemistry, Saarland University, Campus B2 2, D-66123 Saarbrücken, Germany
[2] Center for Mechatronics and Automation, Gewerbepark Eschberger Weg, Geb. 9, D-66121 Saarbrücken, Germany
[3] Institute of Production Engineering, Saarland University, Campus A4 2, D-66123 Saarbrücken, Germany
[*]E-mail: h.natter@mx.uni-saarland.de

Received: 24 March 2015 / *Accepted:* 4 May 2015 / *Published:* 27 May 2015

The corrosion behavior and the electrochemical dissolution of three different cast iron types and one high purity iron sample in $NaNO_3$ electrolyte (25°C, 1 M, pH: 7) were investigated by comparing three different cell setups: a relatively simple beaker-cell, a small-sized capillary flow-cell and a high-current gap-cell. The electrochemical cell types differ in electrolyte flow rate, size of the measured sample surface and applied current density. The work aims at investigating the electrochemical dissolution of inclusion containing materials (cast iron) and the evolution of a strategy that allows the determination of process parameters used for the design of electrochemical machining (ECM) processes. All samples were characterized by X-ray diffraction, energy-dispersive X-ray spectroscopy and scanning electron microscopy. Electrochemical characterization was carried out by cyclic voltammetry and chronoamperometry experiments. It could be shown that the electrochemical dissolution behavior was dominated by the matrix structure and the geometry of the included graphite particles. The determination of corrosion potential and -current were mainly influenced by the electrolyte flow rate. Our new flow cell design (gap-cell) is suited for an easy and fast electrochemical characterization of materials under high current densities.

Keywords: Electrochemical dissolution, cast iron, cyclic voltammetry, ECM application

1. INTRODUCTION

Due to their properties [1, 2], like hardness, chemical and thermal resistivity, cast irons play an important role in modern manufacturing processes [3–6]. Their material- and electrochemical properties are affected by their chemical composition, phase composition and -morphology [7–10]. They are classified by the crystal structure of the iron-matrix and the morphology of the graphite

inclusions. The crystal structure of the matrix consists of ferrite (α-Fe), perlite (alternating ferrite (Fe) and cementite (Fe_3C) layers) or a mixture of ferrite and perlite. Additionally, alloying elements (e.g. Si, Mg, P or S) are present in the matrix. Depending on the graphite morphology [11], according to DIN EN ISO 945 [12], cast irons are divided in six different groups [13−15]. In the present work cast irons with lamellar and spheroid carbon structures are considered.

New casting technologies enable the tailoring of their properties to specific applications and their low price makes them even more interesting. A well-known example is the common rail [16−18] diesel injection system used for automotive applications. Parts of this system were produced by electrochemical machining (ECM). ECM [19–22] is a manufacturing technique that allows a nearly heat-free processing of a wide range of materials. In contrast to conventional methods like turning or drilling, tool and workpiece are spatially separated, being characteristic of the so-called non-conventional methods. Advantages of the ECM process are less tool wear resulting from the non-contact working mode and the manufacturing of complex and/or three-dimensional shapes and geometries [23]. The machinability of the materials is not influenced by the mechanical properties (e.g. hardness, ductility) of the workpiece, but physicochemical properties, like electrical- or heating conductivity, which have to be considered by choosing optimal process parameters. Hence, ECM can be applied to almost every metal or alloy: titanium [24, 25], super-alloys [26] or stainless steel [27]. A further advantage of this technique is the small number of working steps [28, 29] which are required for the manufacturing of complex products. ECM is based on the principle of electrochemical dissolution: a voltage is applied between workpiece (working electrode, WE) and tool (counter electrode, CE). The anodic polarization of the WE leads to its oxidation (dissolution). A flowing electrolyte between the electrodes removes solid and gaseous reaction products. The structure of the CE is negatively transferred to the WE. Typically gap sizes between WE and CE are 1 mm or less. A smaller gap leads to a higher precision, while it simultaneously implies a worse removal of heat- and reaction products [20, 30, 31].

Before designing a new production process by ECM, all electrochemical basic information of the used material has to be available. In most cases these electrochemical quantities are determined in laboratory scale experiments. Numerous information about the electrochemical dissolution of pure metals and alloys [32–36] is available in literature but less information about metal matrix composites [37]. In the present study we discuss the influence of different cell designs on the determination of the corrosion- and dissolution behavior for three cast iron types. Cells with flowing (micro- and gap-cell) and stirred electrolyte (beaker-cell) as well as micro- and macro-sized cells were investigated. Aqueous solutions of $NaNO_3$ or NaCl are widely used and have established as common standard in industrial processes [38]. For this reason the investigations in this work were performed in 1 M $NaNO_3$ solutions (conductivity: 65 mS cm^{-1}, pH: 7) at room temperature.

2. EXPERIMENTAL SETUP

2.1. Sample preparation and -characterization

In the present study three cast iron samples purchased from the Mittelrheinische Metallgießerei H. Beyer GmBH & Co. KG (Andernach, Germany) and a high-purity Armco iron sample (Sigma-

Aldrich, Taufkirchen, Germany) were used. The carbon particle structure and the composition of the iron matrix of the cast iron and iron samples are given in Table 1.

Table 1. Characterization of the used sample materials

Sample	Trade name	Carbon structure	Matrix composition
LFP	EN-GJL-250	lamellae	ferrite-perlite
SFP	EN-GJS-600-3	spheroid	ferrite-perlite
SF	EN-GJS-400-15	spheroid	ferrite
Armco	Armco	–	ferrite

The topology of the surface, the elemental composition and -distribution were determined by scanning electron microscopy (SEM) using a JEOL microscope JSM-7000F (JEOL Ltd., Tokyo, Japan) in secondary electron imaging (SEI) mode (accelerating voltage: 20 kV).

Chemical impurities of the samples were analyzed by inductively coupled plasma–optical emission spectroscopy (Varian 720-ES, Varian Inc., Palo Alto, California). The sample was mechanically ground into a fine powder. 527 mg of the prepared powder were dissolved in a mixture of 10 mL H_2O_2 (33 wt%) and 24 mL HCl (36 wt%) under moderate stirring and heating (60 °C). The resulting solution was diluted with 54 mL H_2O (analysis grade). An analysis solution with a concentration of 1 vol% was prepared by addition of diluted nitric acid (1 wt%). The chemical composition of the sample was analyzed with a multi-element standard (Merck KGaA, Darmstadt, Germany). For a better accuracy of the carbon content hot extraction analysis (elemental analysis) was performed (Vario EL cube, Elementar Analysensysteme GmbH, Hanau, Germany). In a first step the samples were combusted at 1800 °C in an oxygen stream, followed by a separation of the combustion products and a final IR analysis (infrared spectroscopy) of the carbon dioxide amount, which is equivalent to the carbon content.

2.2. Electrochemical cells

The electrochemical measurements were performed in three different cell setups:

1. The beaker-cell consists of a simple cylindrical glass beaker (volume: 400 mL). WE (iron samples) and CE (platinum sheet) are installed in a distance of 50 mm. All potentials are measured vs. Hg/Hg_2SO_4 RE (0.5 M H_2SO_4). The electrolyte was moved with a magnetic stirrer. The WE consists of cubic ($1\times1\times1$ cm^3) cast iron/pure iron samples. Five sides of the cube were electronically insulated with a non-conductive coating; the remaining side (area: 1 cm^2) was used for the measurements.

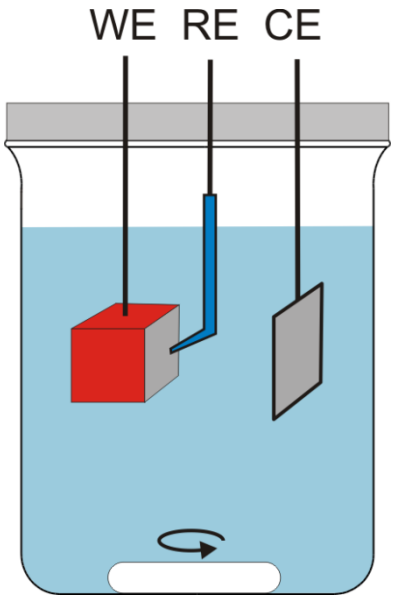

Figure 1. Beaker-cell with a three-electrode setup

2. The constructed micro-cell with a three-electrode setup (CE: platinum wire, RE: Hg/Hg_2SO_4 (0.5 M H_2SO_4)) bases on a concept of Lohrengel et al. [40, 41]. A sketch of the cell is shown in Fig. 2.

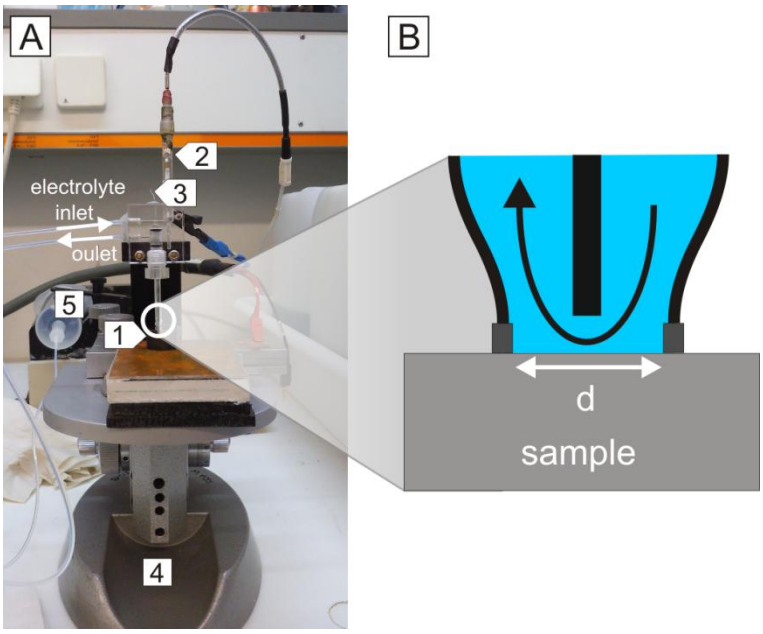

Figure 2. (A) Experimental micro-cell environment (1: sample, 2: reference electrode, 3: counter electrode, 4: mechanically-driven sample stage, 5: syringe pump) and (B) sketch of the θ-capillary mounted onto the sample surface.

A θ-capillary enables the investigation of a very small sample area (13 mm^2). The application of moderate potentials (5-10 V) leads to enormous current densities which are comparable to the conditions in an ECM production plant. One half of the θ-capillary is used as electrolyte inlet. At the

end of the capillary (see Fig. 2) the electrolyte overflows the WE and streams out of the opposite side. The interface between capillary and sample is sealed with a silicone O-ring. The CE is located in the outlet channel of the capillary. Two types of capillaries with different active sample surfaces were used. The effective electrode area (capillary 1: 0.78 mm^2, capillary 2: 2.51 mm^2) was determined by measuring the corroded area of the sample with an optical microscope (SMZ800, Nikon Corporation, Tokyo, Japan). The active sample areas used for the calculation of the current density j were received by averaging the results of four single measurements. The electrolyte (1 M $NaNO_3$, pH: 7, T: 25°C) was pumped through the system with a syringe pump. Three different flow rates were applied: 1 mL min^{-1}, 5 mL min^{-1} and 9 mL min^{-1}.

3. In this new cell design samples can be measured under high current densities. The enormous electrolyte flow was realized by pressing the electrolyte through a curved flow channel with gradually decreasing diameter (Fig. 3). The parts of the flow cell were manufactured in a 3D printing process. The sample holder consists of stainless steel and enables the electronic contact to the sample. A cross section and an exploded view drawing of the gap-cell are shown in Fig. 3 and 4.

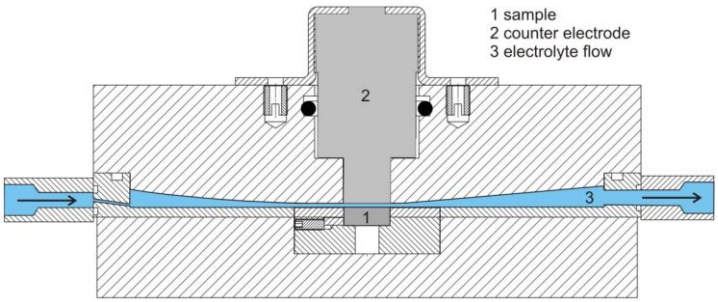

Figure 3. Vertical cross-section of the gap-cell along the electrolyte flow channel

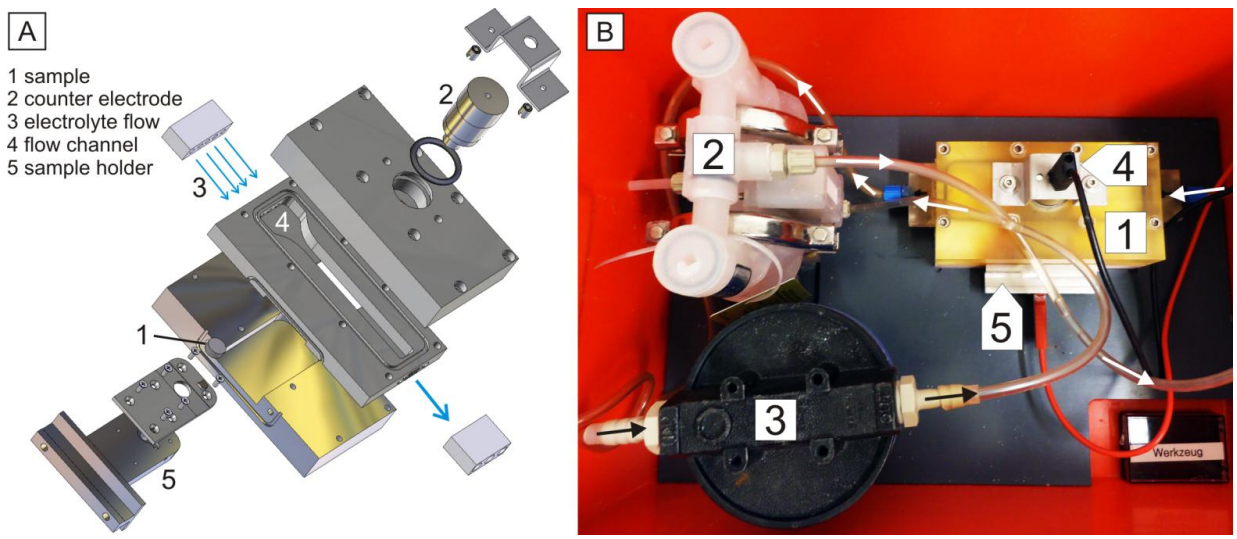

Figure 4. Exploded view drawing (A) of the gap-cell cell and the experimental setup (1 gap-cell, 2 high pressure pump, 3 particle filter, 4 counter electrode, 5 sample holder with working electrode, black and white arrows indicating the electrolyte flow)

The electrolyte gap between sample and counter electrode can be adjusted by positioning the counter electrode with a micrometer screw. For the present experiments the gap size is 100 μm. The cylindrical samples with a surface of 1 cm^2 and a height of 5.2 mm were mechanically manufactured. The counter electrode consists of stainless steel (diameter: 12.8 mm). The electrolyte was pumped with a compressed-air pump at a flow rate of 600 mL min^{-1}. For recovering the electrolyte a micro filter was installed in the electrolyte circuit. In contrast to the other cells, the present gap-cell setup is running in two-electrode mode without an RE.

The main advantage of the gap-cell is the realization of technical process parameters especially for electrochemical machining processes. Using a micro-structured counter electrode the setup allows also a structuring of the working electrode. In this case the reproduction accuracy can be measured. The distance between WE and CE is fixed and very small, the electrolyte flux can be varied.

2.3. Electrochemical measurements

Cyclic voltammetry- (CV) and chronoamperometric (CA) measurements with the micro- and beaker-cell were performed with a BioLogic SP150 potentiostat (BioLogic SAS, Claix, France) whereas high current investigations with the gap-cell required a BioLogic VMP3 potentiostat with a BioLogic VMP3 B10 booster. The data was collected with the EC-Lab V10.37 software. All measurements were performed in 1 M $NaNO_3$ (pH: 7) at 25° C. For the CV experiments the sweep rate was set to 20 mV s^{-1} (micro- and beaker-cell), respectively, 100 mV s^{-1} for the gap-cell. LFP, SFP and SF were measured in the micro- and beaker-cell (three-electrode setup) in a potential range from −1.5 to – 0.4 V (vs. Hg/Hg_2SO_4) whereas Armco was measured in the micro- and beaker-cell between –1.5 to 1.5 V (vs. Hg/Hg_2SO_4). The voltage range for the polarization experiments in the gap-cell was set to −4 – +10 V (two electrode setup). For reproducibility reasons the micro- and beaker-cell experiments were repeated 10 times and the gap-cell measurements 3 times. The corrosion potentials (E_{corr}) were determined by a Tafel-evaluation. In the case of the micro- and beaker-cell CA traces were recorded at a potential of −0.6 V (vs. Hg/Hg_2SO_4) for 10 min, respectively, and at 6 V for the gap-cell measurements (5 min). The experiments in the micro- and beaker-cell were repeated 10 times, the gap-cell experiments were performed once.

The samples were ground with abrasive paper in the order 500, 800, 2800 and 4000. Before each electrochemical measurement the samples were dipped into HCl solution (1 M) for 10 s to remove oxide layers. Finally, the samples were washed with deionized water and dried in air.

3. RESULTS AND DISCUSSION

3.1. Structural and chemical analysis

3.1.1. Scanning electron microscopy

The used series of samples show significant differences in their matrix structure and in size/morphology of their graphite inclusions. For comparison reasons and the interpretation of the graphite-particle influence on the electrochemical dissolution behavior a high-pure iron sample

(Armco) was measured. First of all the morphology of the graphite inclusions was measured by SEM. Electron microscope images of the samples are shown in Fig. 5. The images with high magnification (Fig. 5 d, e, f) illustrate the size and the distribution of the carbon particles in the matrix phase.

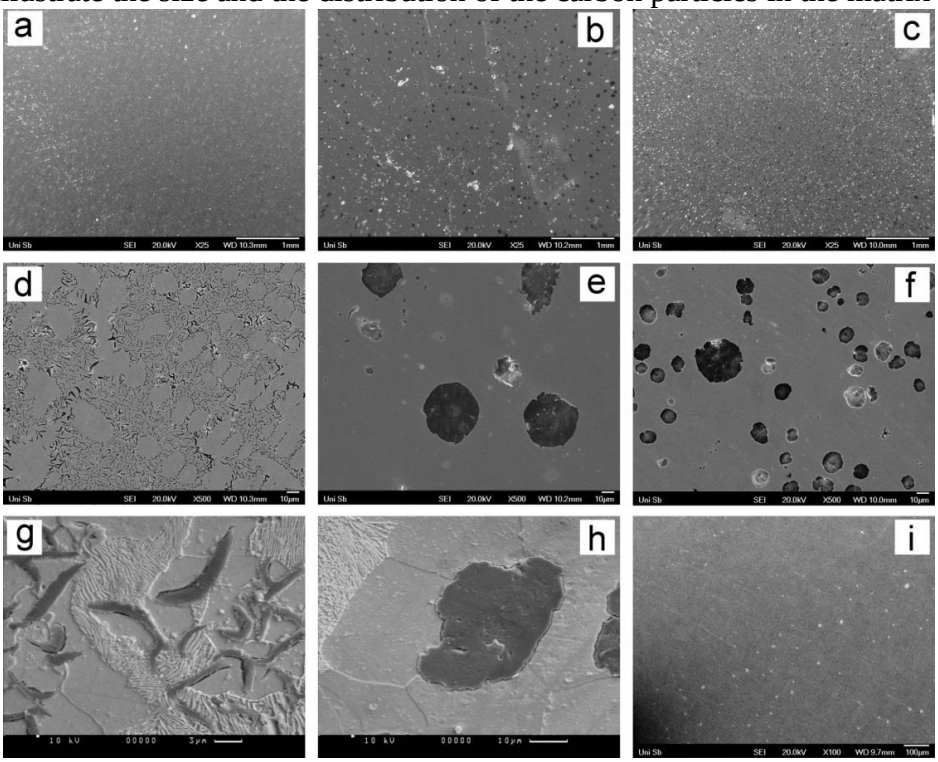

Figure 5. SEM images of LFP (a,d,g), SFP (b,e,h), SF (c,f) and Armco (i)

LFP shows the smallest carbon particles of all measured samples. The carbon lamellae have a length of 1-2 µm and a diameter of 50-100 nm. The spherical particles in SFP have a diameter of 40-70 µm whereas the graphite spheres in SF are smaller (10-30 µm). The distribution and the degree of agglomeration of the graphite particle were measured by EDX element mapping. The results are shown in Fig. 6. The element mappings reveal a statistical distribution of the lamellae dispersed in the matrix of ferrite and perlite as well as of the spheres in sample SFP and SF. Some areas of high or low particle concentrations can be found in all samples (Fig. 6).

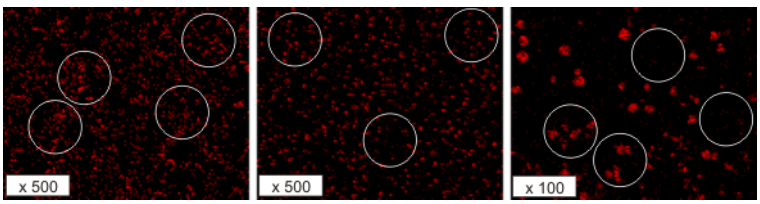

Figure 6. Element mapping of graphite particles (LFP: left, SFP: middle, SF: right). White circles indicate regions with an inhomogeneous particle distribution.

3.1.2. Chemical composition and crystalline phases

It is known that the electrochemical dissolution behavior depends on the chemical composition [32, 42, 43]. For this reason it was determined by different analysis methods. The results are given in Table 2. The content of graphite (3.2 – 3.3 wt%) and the alloying elements are within the specification according to ASTM (American society for testing and materials) standards (A48/A48M-03, A536-84, A897/A897M-06). The crystalline structure of the measured cast iron types has recently been published by Weber et al. [44]. The following phases were found: 14 % ferrite, 83% cementite (Fe_3C) for LFP, 3% iron-silicon, 11% ferrite, 85% cementite, 4% austenite for SFP and pure ferrite for SF. Perlite is a phase mixture of ferrite and cementite and consists of a finely-striped lamellae structure (Fig. 5 g,h). The metallic impurities, like Al, Mn, Co, Ni and P, are located in the iron crystal lattice on regular lattice- or on interstitial sites. Silicon forms an additional iron silicon phase ($Fe_{0.42}Si_{2.67}$).

Table 2. Chemical compositions of the measured samples. Suspended numbers indicate the analysis method

Content / wt%	LFP	SFP	SF	Armco
C	3,20[2]	3,50[2]	3,30[2]	0.01[2]
Al	0,60[1]	0,60[1]	0,70[1]	0.06[1]
Si	1,80[1]	3,00[1]	3,10[1]	0.03[1]
P	0,39[1]	0,28[1]	0,33[1]	0.05[1]
Mn	0,58[1]	0,19[1]	0,19[1]	0.06[1]
Fe	92,30[1]	91,30[3]	90,90[3]	99.72[1]
Co	0,80[1]	0,50[1]	0,90[1]	0.05[1]
Ni	0,08[1]	0,30[1]	0,30[1]	0.01[1]
Cr	0,07[1]	0,07[1]	0,06[1]	u.d.
Cu	0,11[1]	0,10[1]	0,06[1]	0.01[1]
S	0,07[1]	0,03[1]	0,03[1]	0.03[1]

[1] determined by inductively coupled plasma optical emission spectroscopy (ICP−OES)

[2] determined by hot extraction analysis

[3] determined by EDX

[u.d.] under detection limit

3.2. Electrochemical dissolution behavior measured by cyclic voltammetry

3.2.1. CV measurements in the beaker-cell

The beaker-cell has the simplest design of the three measured electrochemical cells. A magnetic stirrer bar moves the electrolyte in the cell, causing a weak electrolyte stream at the surface of the working electrode. The moved electrolyte enables the detachment of gas bubbles and loosely bound reaction products, like iron oxides, hydroxides, and dissolved graphite particles.

Typical cyclic voltammogramms are presented in Fig. 7. E_{corr} values −1196 mV (vs. Hg/Hg_2SO_4) for LFP, −1036 mV (vs. Hg/Hg_2SO_4) for SFP, −995 mV (vs. Hg/Hg_2SO_4) for SF and −807 mV (vs. Hg/Hg_2SO_4) for Armco were received from the Tafel-evaluation [45, 46], as shown in Fig. 8.

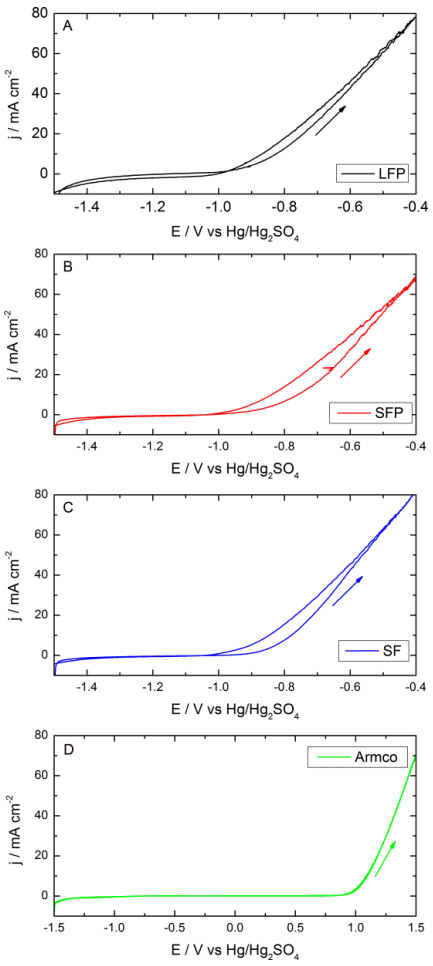

Figure 7. Cyclic voltammogramms of LFP, SFP, SF and Armco samples measured in 1 M $NaNO_3$ at pH 7.

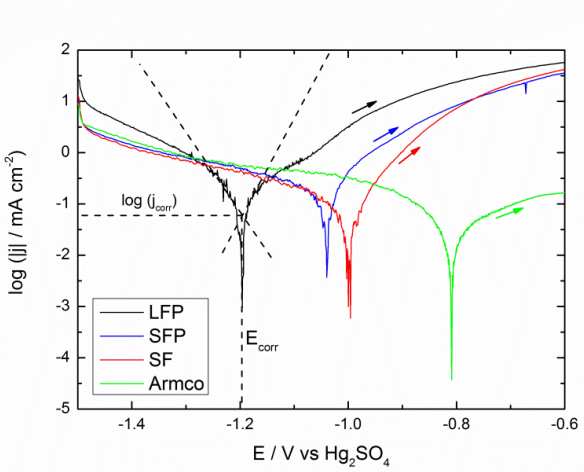

Figure 8. Determination of E_{corr} and j_{corr} according to the Tafel-evaluation

The gas evolution is vigorous for current densities above 100 mA cm^{-2} and leads to a very noisy signal. For this reason this kind of cell setup is only suited for equilibrium- and low current measurements. Significant differences in E_{corr} values can be observed. The LFP cast iron with the lamella shaped graphite has the highest negative free corrosion potential, followed by SFP, SF and Armco. This sequence of corrosion stability can be explained by the matrix structure and the size and shape of the graphite particles. It could be shown [44, 47, 48] that the concentration of the electric field lines at the peaks and edges of the lamella shaped structures is responsible for the different dissolution mechanisms. Fig. 9A shows a high-resolution scanning electron micrograph of a graphite lamella (matrix: ferrite/perlite).

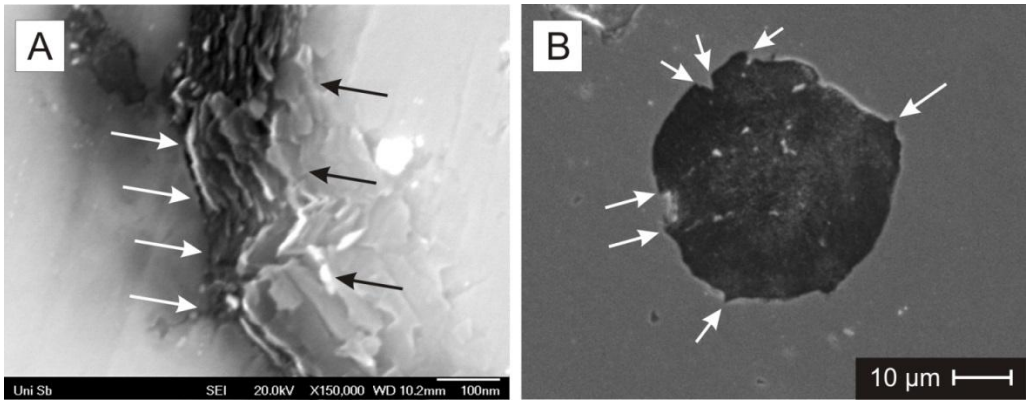

Figure 9. High-resolution scanning electron micrograph of LFP (A) and graphite sphere of SFP (B). The arrows indicate areas of a high electric field-lines density

SFP consists of a lamella-shaped perlite matrix (Fig. 5 h) and nearly regular-shaped graphite particles with only a few edges and peaks (Fig 9 B, white arrows) which lead to the same effects as described for LFP. SP is a composite of spherical graphite particles in a ferrite matrix and Armco iron does not have any structural inhomogeneities. The order of the E_{corr} values corresponds to the type and number of structural inhomogeneities. These results could recently be confirmed by FEM (finite element method) simulations [49].

3.2.2. CV measurements in the micro-cell

The micro-cell setup has been developed for electrochemical dissolution measurements with high currents and for measuring small sample areas. A flowing electrolyte removes all gaseous and solid reaction products from the surface of the working electrode. The controlled electrolyte flow is a decisive advantage of the micro-cell setup.

In a first series of tests, CV measurements were performed in a potential range of −1.5 to −0.4 V (vs. Hg/Hg_2SO_4). The resulting current densities are in the order of 20 mA cm^{-2} (Fig. 10, 11). Compared to the beaker-cell the resulting current densities are reduced by a quarter or third, resulting from a strong ohmic drop caused by considerable distance between working- and reference electrode.

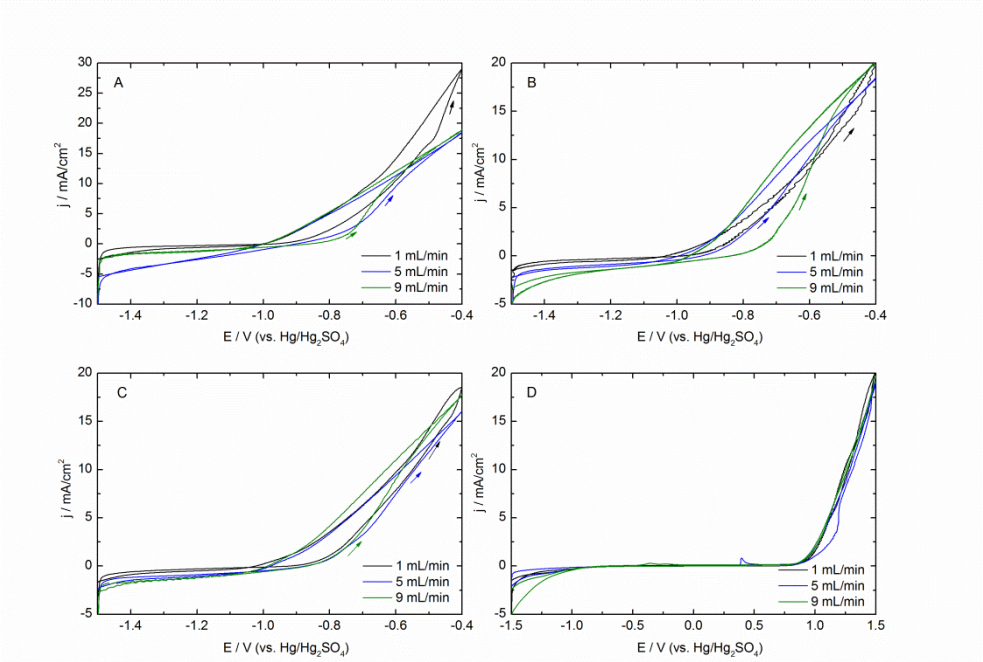

Figure 10. Cyclic voltammogramms measured in the micro-cell with capillary 1 (A: LFP, B: SFP, C: SF, D: Armco)

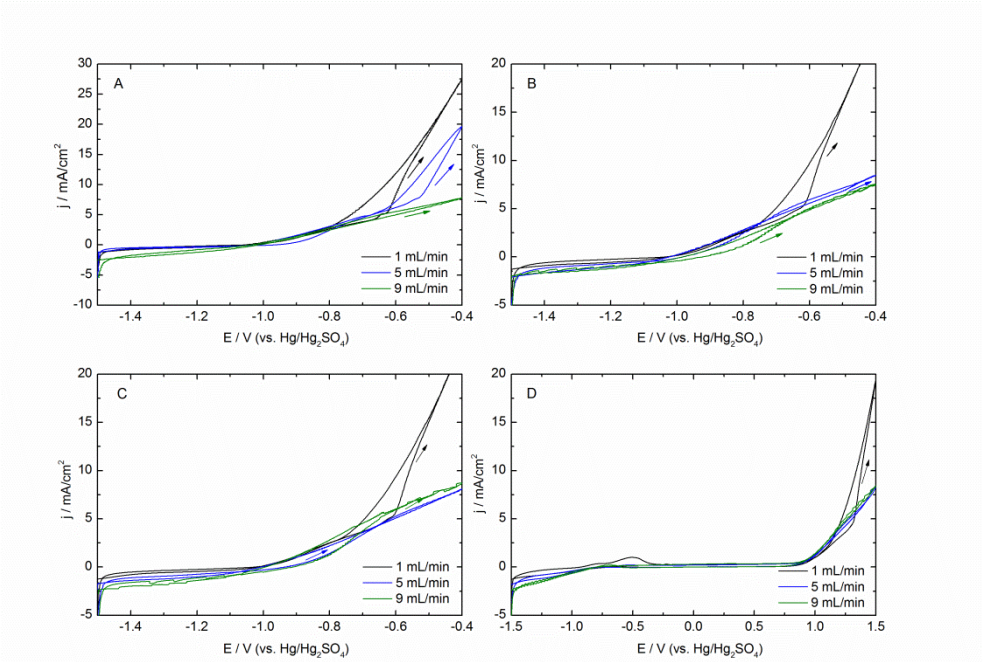

Figure 11. Cyclic voltammogramms measured in the micro-cell with capillary 2 (A: LFP, B: SFP, C: SF, D: Armco).

The forward scans of the CV measurements with different electrolyte flow rates and capillary diameters were evaluated according to the Tafel-procedure described in Sect. 3.2.1. The corrosion potentials are summarized in Table 3.

Table 3. E_{corr} and j_{corr} values measured in the micro-cell setup with different capillary diameters and under different electrolyte flow rates. The measured potentials refer to the Hg/Hg_2SO_4 reference electrode

WE size: 0.78 mm^2						
Flow / mL min^{-1}	1		5		9	
	E_{corr} / mV	j_{corr} / μA mm^{-2}	E_{corr} / mV	j_{corr} / μA mm^{-2}	E_{corr} / mV	j_{corr} / μA mm^{-2}
LFP	−965	0.252	−898	0.407	−865	0.324
SFP	−975	0.154	−900	0.412	−850	0.392
SF	−940	0.093	−864	0.280	−853	0.414
Armco	−792	0.074	−693	0.061	−727	0.065
WE size: 2.51 mm^2						
LFP	−1012	0.235	−996	0.566	−974	0.593
SFP	−1010	0.135	−970	0.471	−918	0.483
SF	−1000	0.096	−926	0.360	−915	0.450
Armco	−870	0.142	−803	0.138	−787	0.102

Three observations were derived from summarizing Fig. 10, 11 and Table 3:

1. For capillary 2 and high flow rates E_{corr} shifts to more positive values in the following order: LFP→ SFP →SF →Armco

2. E_{corr} values measured with capillary 2 differ strong from the series of measurements using capillary 1,

3. j_{corr} values measured with capillary 1 show a weak electrolyte flow dependency whereas j_{corr} values measured with capillary 2 are strongly increased at high flow rates (5 and 9 mL min^{-1}).

As discussed above, the order of the E_{corr} values of the cast iron- and pure iron samples can be explained with the geometric structure of the matrix and the graphite particles. Armco iron without any graphite particles has an extended passive region followed by a transpassive dissolution whereas the cast irons show a complete different dissolution being nearly active. In the case of the cast irons the graphite inclusions disturb the formation of a passive layer and therefore lead to a diminution of the energy needed for dissolution, i.e. E_{corr}. The carbon-iron matrix interfaces also lead to an amplification of the local current density which correlates with a diminution of E_{corr}. Furthermore, the order of E_{corr} of the cast iron samples depends on the electrolyte flow and the capillary diameter.

E_{corr} shifts to more positive values with increasing electrolyte flow − irrespective of the observed material and the capillary diameter. The observation can be explained with the different matrix structures of the cast irons. For capillary 2 the difference in the E_{corr} values of SF and SFP is smaller compared to E_{corr} of LFP. SFP and LFP have a matrix with a perlite fraction; the LFP graphite lamella generates additionally inhomogeneities in the electric field whereas SF and Armco consist of pure ferrite. The flow rate dependency of E_{corr} can be explained with the removal behavior of the electrolyte stream. The passivation or blocking of the electrode surface caused by reaction products (iron oxides, hydroxides, adsorbed oxygen species) is much easier at low flow rates which lead to an increase of E_{corr}. This effect is very significant for the ferritic-perlitic cast irons types (LFP and SFP).

E_{corr} values depend on the diameter of the used capillary. A decreasing capillary diameter, i.e. a smaller WE surface, leads to an unsystematic evolution of the E_{corr} values as function of the electrolyte flow. The explanation for this behavior could be the influence of an inhomogeneous graphite particle distribution. Fig. 12 shows a series of ten CV experiments with the micro-cell setup (1 mol/L $NaNO_3$ electrolyte, scan range −1.4 and 0.6 V (vs. Hg_2SO_4), scan rate: 100 mV s^{-1}, T: 25°C, pH: 7) and the corresponding graphite particle distribution for experiment 7 and 10 measured by scanning electron microscopy.

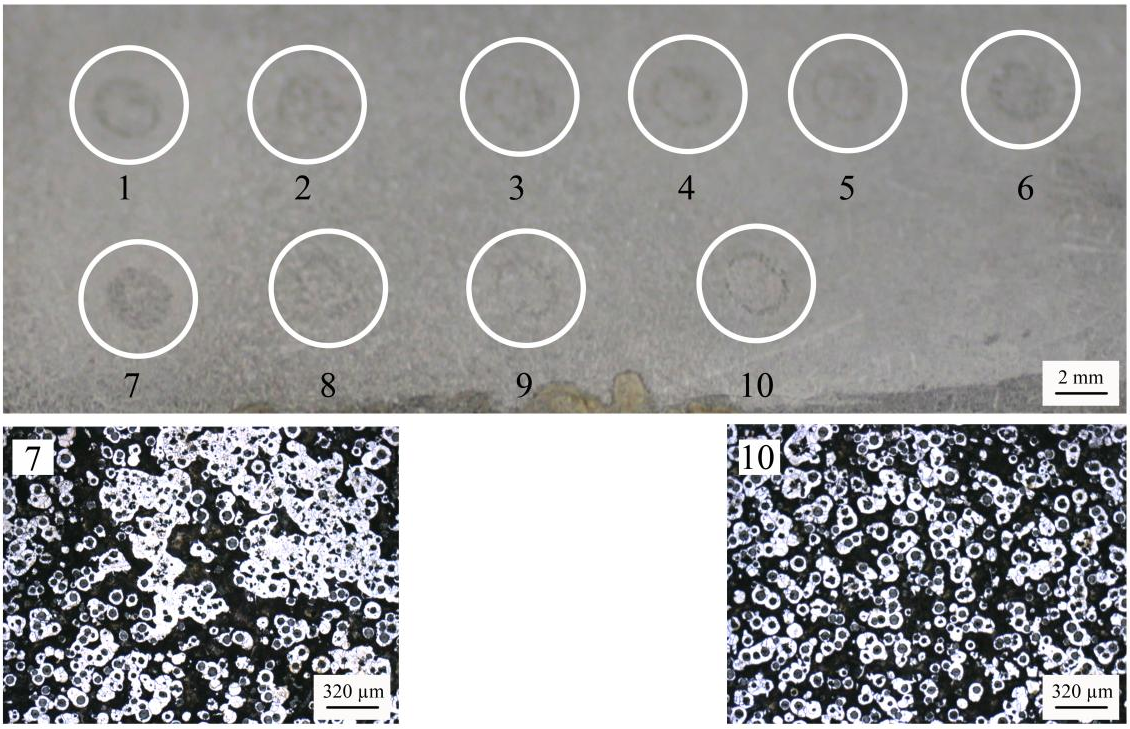

Figure 12. Series of CV experiments with a micro-cell setup (capillary 2) and electron micrographs of experiment 7 and 10.

It can be observed that the graphite particle distribution is quite different for the measured positions. Position 7 shows some large agglomerates whereas the graphite particles at position 10 are homogeneously distributed. The smaller the capillary size the greater is the influence of inhomogeneities on the measured corrosion potentials. Armco iron without any graphite particles does not show a significant capillary dependency on E_{corr} whereas a dependency on the electrolyte flow can be observed. Increasing potentials increase the dissolution rate of iron accompanied by an increased formation of reaction products. The measured current densities depend also on the electrolyte flow rate. The highest current densities could be observed for 9 mL min^{-1}, supporting the presented explanations for the capillary-size- and electrolyte-flow dependency observed in micro-cell experiments.

3.2.3. CV measurements with the gap-cell

CV experiments in this experimental device cannot be performed in a three-electrode setup. For this reason the obtained results are not directly comparable to those of the micro- and beaker-cell. The two-electrode setup without a reference electrode leads to a different potential scale. For this reason the received results represent a trend for the electrochemical dissolution of the different materials. The measured cyclic voltammogramms are presented in Fig. 13. LFP dissolves at −2,701 V, SFP at −2,751 V, SF at −2,570 V and Armco at −2,890 V.

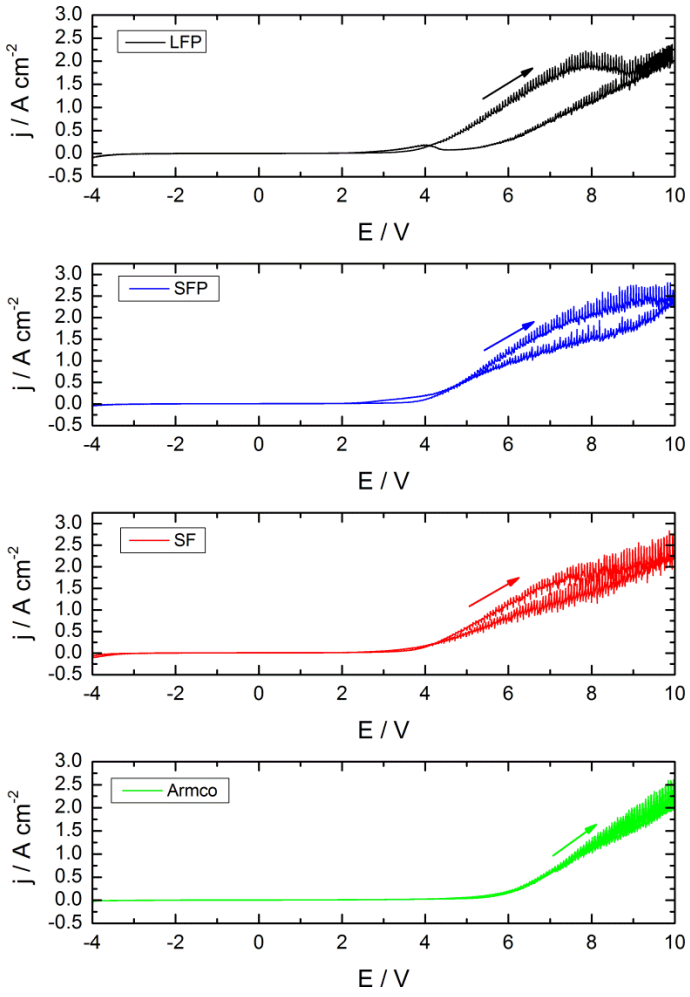

Figure 13. Potentiodynamic scans measured in the gap-cell. The experiments were performed in a two electrode setup (internal electronic reference) with an electrolyte flow rate of 600 mL min^{-1}

The relatively high negative E_{corr} value of the Armco sample may result from the formation of a thin passivation film accompanied by oxygen evolution. In contrast to the cast iron samples which formed thin black films on their surface, the surface of Armco iron looked unaffected. SFP and LFP have comparable dissolution potentials whereas SF dissolves at a more positive E_{corr} value. The fast dissolution behavior of LFP and SFP can be explained by lamellar perlite structures (see Sect. 3.2).

3.3. Electrochemical dissolution of cast iron measured by chronoamperometry

3.3.1 Chronoamperometry measurements performed in the beaker-cell

Chronoamperometric measurements in a three-electrode setup were performed to investigate the time dependency of the dissolution process. After applying a constant voltage, the dissolution of the cast iron and parallel side reactions (gas formation, oxide- and hydroxide formation) lead to a time-dependent current j_{lim}. The magnitude and the time dependency of j_{lim} depend on:

i) the experimental setup (electrolyte flow),

ii) the experimental conditions (pH, applied voltage, T) and

iii) the sample material.

The beaker-cell has a vertical electrode arrangement that allows an unimpeded detachment of the gas bubbles supported by a weak electrolyte flow resulting from the magnetic stirrer.

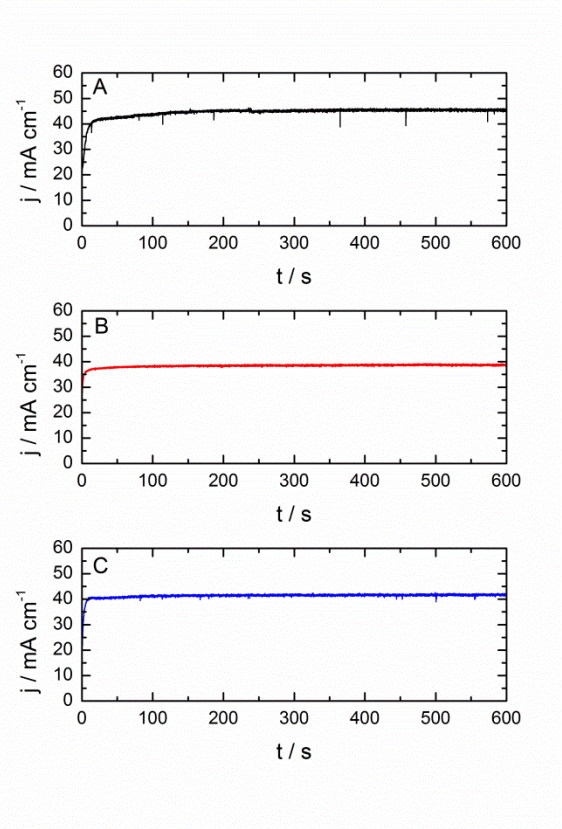

Figure 14. Chronoamperogramms of LFP (A), SFP (B) and SF (C) measured in the beaker-cell setup

Advantages of the beaker cell are the large sample area (minimizing the influence of inhomogeneities) and the small distance between RE and WE (reducing the RI drop). The decisive disadvantage of this setup is the weak and uncontrollable electrolyte movement that does not allow experiments with high dissolution voltages. For this reason a relatively small dissolution voltage of −0.6 V (vs. Hg/Hg_2SO_4) was used. The measured chronoamperogramms are presented in Fig. 14. After an initial period of 10−20 s j_{lim} reaches the maximum and stays nearly constant during the investigation of 600 s. The values of j_{lim} are 45 mA cm^{-2} for LFP, 39 mA cm^{-2} for SFP and 41 mA cm^{-2} for SF. LFP

has the highest j_{corr} value due to the large surface area of the very small graphite lamella. As discussed above, an increased dissolution takes place at the peaks and edges of the lamella due to the concentration of the electric field lines. This effect is quite smaller for SFP and SF, resulting in decreased j_{corr} values.

3.3.2 Chronoamperometry measurements performed in micro-cells

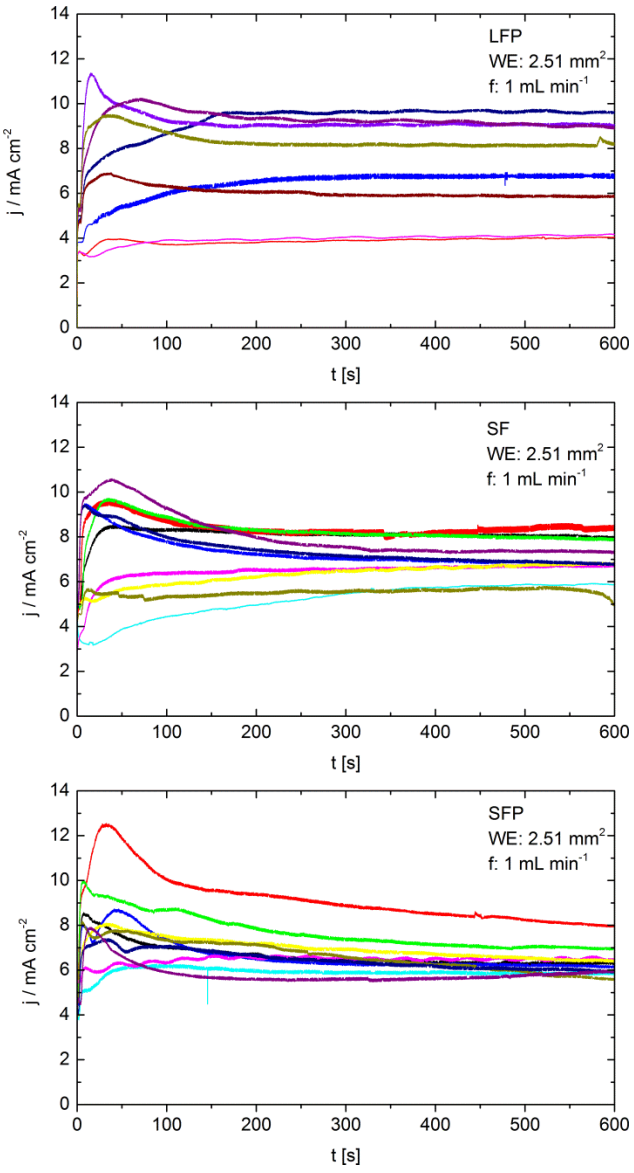

Figure 15. Series of ten chronoamperogramms measured in the micro-Cell with capillary 2 and an electrolyte flow (f) of 1 mL min^{-1}.

An effective electrolyte flow removes solid and gaseous reaction products from the electrode surface. For testing the influence of the electrolyte flow on the cast iron dissolution, experiments with different flow rates were performed in a micro-cell with capillary 2. As shown in Sect. 3.2.2, for homogeneity reasons smaller capillary diameters are not suited for the dissolution of cast iron. A

dissolution voltage of −0.6 V (vs. Hg/Hg_2SO_4) was used for a series of experiments. Fig. 15 shows a bad reproducibility of j_{lim} at an electrolyte flow of 1 mL min^{-1}. It varies between 4 and 12 mA cm^{-2} and the time dependency also scatters. This effect results from the capillary geometry that leads to an agglomeration of removed graphite particles and reaction products at the outlet of the capillary. Especially in the case of a slow electrolyte flow, the particle blockage leads to irreproducible measurements. Another reason for this result is the formation of local passivation layers due to the ineffective removal of reaction products. For high electrolyte flow rates this effect should be reduced. Experiments with flow rates of 5 and 9 mL min^{-1} are shown in Fig. 16. A flow rate of 9 mL min^{-1} leads to a sufficient removal of the reaction products which impede the electrolyte flow and remove passivation layers from the WE.

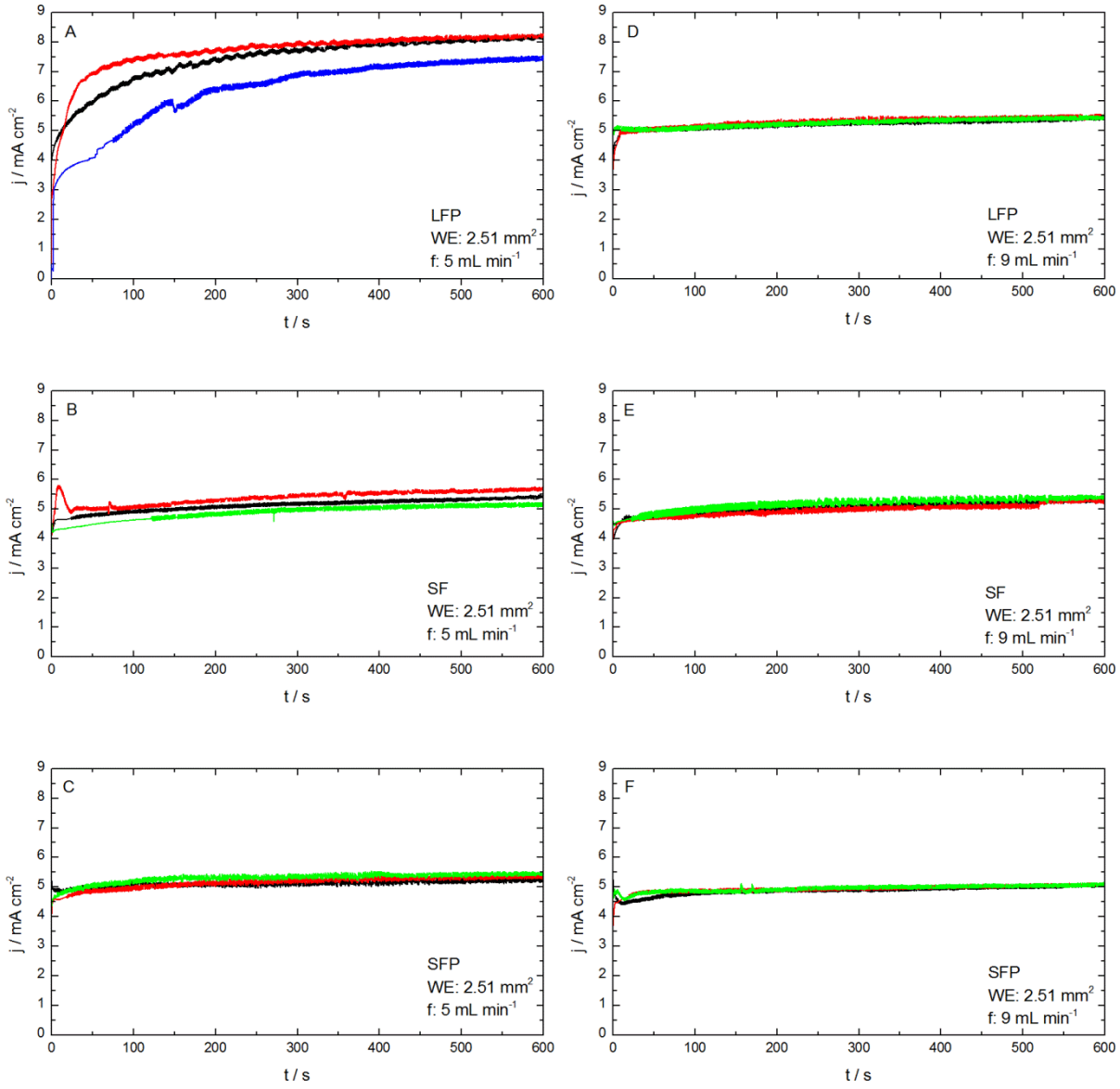

Figure 16. Series of three chronoamperogramms measured in the micro-cell with capillary 2 and an electrolyte flow of 5 mL min^{-1} (A-C) and 9 mL min^{-1} (D-F)

Fig. 16 A-C shows an improvement of the experimental reproducibility. A further increase of the electrolyte flow rate (Fig. 16 D-F) leads to good reproducibility. After 500 s, a j_{lim} value of 5.52 mA cm^{-2} was measured for LFP, 5.14 mA cm^{-2} for SFP and 5.11 mA cm^{-2} for SF. The order of the determined j_{lim} values corresponds to the microstructural compositions of the cast irons and the related dissolution behavior.

Especially at low electrolyte currents, the reproducibility of the measurements is very bad. Another problem is the removal of solid particles, reaction products and the formation of gas bubbles which block the capillary and disturb the measurement significantly. Higher flux rates reduce these problems but sophisticated sealing concepts are necessary. In this work we could confirm the practical applicability of the micro-cell setup for measuring pure materials but electrochemical measurements on metal-matrix composites have to be performed very carefully with regard to the electrolyte flux and the sample homogeneity. Therefore, the micro-cell is an electrochemical standard device which is very suitable for material investigations and parameters analysis. Furthermore, additive manufacturing techniques like 3D printing facilitate the construction of durable and sophisticated micro-cells.

3.3.3 Chronoamperometric measurements with high dissolution currents

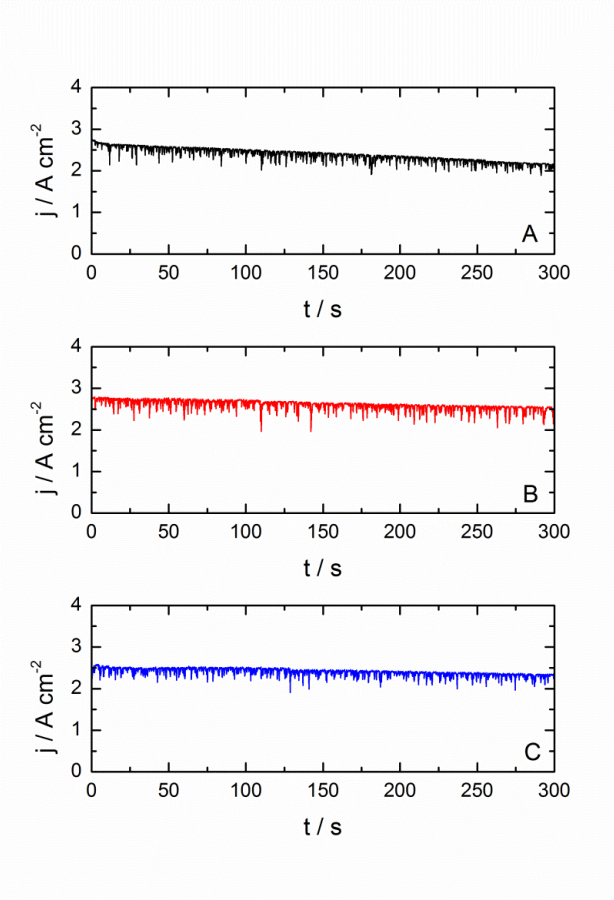

Figure 17. Chronoamperogramms measured in the gap-cell (A: LFP, B: SFP, C: SF) with an applied voltage of 6 V and an electrolyte flow of 600 mL min^{-1}

Beaker- and micro-cell were used for measurements with low and moderate dissolution currents. The gap-cell was designed for investigations with nearly technical-like conditions − high current densities, dissolution- and electrolyte flow rates. The high electrolyte flow was realized with a curved flow channel structure in combination with a small gap between CE and WE. A flow rate of 600 mL min^{-1} is able to remove all gas bubbles and reaction products. An additional removal of reaction products from the electrode surface was received by the strong gas evolution due to the formation and growth of gas bubbles in micro cracks of oxide- or hydroxide layers. The present cell design avoids an agglomeration of solid products in the flow channel. The results of chronoamperometric investigations measured with the gap-cell (static two-electrode setup) are shown in Fig. 17.

Armco iron shows an immediate passivation accompanied by a strong current drop. After the experiment, the sample surface looks bright and no significant weight-loss could be observed. Only a small current, resulting from oxygen evolution and not from the dissolution of the sample, was registered during the experiment.

The chronoamperometric measurements of all cast iron samples start with a j_{lim} value of 2.70 A cm^{-2}. The time dependencies of j_{lim} follow nearly straight lines. The slopes of the straights decrease in the order LFP (−0.098 A cm^{-2} s^{-1}) → SF (−0.048 A cm^{-2} s^{-1}) → SFP (−0.038 A cm^{-2} s^{-1}).

The decrease of the slopes can be associated with a high mass removal rate connected to a strong increase of the gap between WE and CE. In contrast to the industrial ECM process, the gap size cannot be kept constant and therefore the resistance increases during the experiment. A comparison of the samples' volume before and after the CA experiments confirms the experimental data. Haisch et al. [42] observed the formation of black iron carbide layers during electrochemical steel dissolution in $NaNO_3$ electrolyte leading to a current-density drop. During the present CA experiments thin black layers were formed which could be the reason for the observed j_{lim} drop. A difference in the formation behavior of these layers between lamellar and spheroidal cast irons could be an additional reason for the different slopes. The current spikes in the measurement result from the used compressed-air pump that causes a pulsating electrolyte flow.

4. CONCLUSION

Three different cell designs are compared in electrochemical dissolution experiments of different cast iron types. The most critical points are the included graphite particles and passivating oxide- or hydroxide layers which influence the electrochemical dissolution of these metal-matrix composites. Therefore, it is obvious that the electrolyte flow is the most important experimental parameters.

The beaker-cell, a relatively simple setup operated in a two- or three-electrode mode, is suitable for all kinds of experiments under low current densities and dissolution rates. The relatively weak electrolyte current is not able to remove gas bubbles and solid reaction products. As demonstrated in this study, basic electrochemical parameters like E_{corr}, or j_{corr} can be determined with very high accuracy. For the investigation of technical processes (e.g. ECM) the use of the beaker-cell is not

recommended. Typically applications for this type of cell are corrosion resistance tests and durability tests of materials in different environments [50−52].

The micro-cell setup developed by Lohrengel et al. has been developed for measurements with a technical background, especially under high current densities associated with vigorous gas evolution. Enormous current densities are achieved by measuring a very small WE area (mm^2 or less). Reaction products, for example oxygen, hydrogen or dissolved ions species, can be analyzed by physical, spectroscopic and chemical methods [53, 54]. The correct application of all these features assumes a homogeneous sample composition given for pure metals or homogeneous alloys. Samples containing insoluble micro particles or inhomogeneous materials with different crystal phases affect the measurement significantly, which has been confirmed in this work.

The gap-cell has the most complex design of the measured cells. The structure of the curved flow-channel enables a very high electrolyte flow through a very small electrode gap. The main advantage of the gap-cell is the realization of technical process parameters especially for electrochemical machining processes. The present results confirm that the process heat and the formation of gas bubbles and reaction products do not affect the measurement. The magnitude of dissolution is very high at the measured electrolyte flux rate.

It could be shown that the use of each cell setup is restricted to special applications. The investigation of the electrochemical dissolution behavior of metal matrix composites and complex-structured materials requires complimentary cell setups and -techniques as well as a proper choice of the experimental parameters.

ACKNOWLEDGEMENTS

We thank the European Commission within the Interreg IV A program “Initiative PRECISE” for financial support, Prof. Dr. Dirk Bähre, Prof. Dr. Rolf Hempelmann and Dr.-Ing. Martin Weinmann for fruitful discussions and Dipl.-Ing. Sylvia Kuhn, Dipl.-Ing. Rudi Richter and Elfi Jungblut for the experimental support.

References

1. S.R. Andoko, A. Purnowidodo, Y.S. Irawan, *Int. J. of Appl. Engineering Research*, 9 (2014) 541
2. R.W. Gregorutti, J.E. Grau, *Int. J. of Cast Metals Research*, 27 (2014) 275
3. J.Y. Lee, H.D. Park, S.J. Kim, J.M. Han, Y.C. Kim, J.D. Lim, J.K. Kim, *SAE Int. J. of Materials and Manufacturing*, 2 (2010) 19
4. J. Rammeisberg, *Wasser und Abfall*, 10 (2008) 44
5. P. Fallböhmer, C.A. Rodríguez, T. Özel, T. Altan, *J. of Materials Processing Technology*, 98 (2000) 104
6. D. A. Karandikar, Resources, *Conservation and Recycling*, 5 (1991) 61
7. E. Lunarska, *Materials and Corrosion*, 47 (1996) 539
8. A. Velichko, C. Holzapfel, A. Siefers, K. Schladitz and F. Mücklich, *Acta Mater.*, 56 (2008) 1981
9. D. Li, L. Liu, Y. Zhang, C. Ye, X. Ren, Y. Yang, Q. Yang, *Materials and Design*, 30 (2009) 340
10. J. Keller, V. Fridrici, Ph. Kapsa, S. Vidaller, J.F. Huard, *Wear*, 263 (2007) 1158
11. X. Yao, X. Feng, Y. Shen, B. Li, J. Zhang, H. Xu, B. Kuang, *Materials and Design*, 65 (2015) 847

12. Mikrostruktur von Gusseisen - *Teil 1: Graphitklassifizierung durch visuelle Auswertung* (ISO 945-1:2008), Beuth Verlag, Berlin (2008)
13. P.C. Pattan, V.D. Mytri, P.S. Hiremath, *Proceedings of SPIE - The International Society for Optical Engineering*, 7546 (2010) 75462S
14. O.D.F.M. Gomes, S. Paciornik, *Microscopy and Microanalysis*, 11 (2005) 363-371
15. A. Velichko, F. Mücklich, *Practical Metallography*, 43 (2006) 192
16. E. Mancaruso, S.S. Merola, B.M. Vaglieco, *Int. J. of Engine Research*, 9 (2008) 483
17. Y. Zhang, A.L. Boehman, *Energy and Fuels*, 21 (2007) 2003
18. T. Tanaka, A. Ando, K. Ishizaka, *JSAE Review*, 23 (2002) 297
19. J.A. McGeough, *Principles of Electrochemical Machining*, Chapman and Hall, London (1974)
20. R. Schuster, V. Kirchner, P. Allongue, G. Ertl, *Science*, 289 (2000) 98
21. M. Datta, D. Landolt, *Electrochimica Acta*, 26 (1981) 899
22. V. Kirchner, L. Cagnon, R. Schuster, G. Ertl, *Applied Physics Letters*, 79 (2001) 1721
23. B. Bhattacharyya, J. Munda and M. Malapati, *Int. J. Machine Tools and Manufacture*, 44 (2004), 1577
24. C. Madore and D. Landolt, *J. Micromech. Microeng.*, 7 (1997), 270
25. D. Clifton, A.R. Mount, D.J. Jardine, R. Roth, *J. of Mater. Processing Technology*, 108 (2001) 338
26. D. S. Bilgi, V. K. Jain, R. Shekhar and S. Mehrotra, *J. Mater. Process. Technol*., 149, (2004), 445
27. E. Rosset, M. Datta and D. Landolt, *J. Appl. Electrochem*., 20 (1990) 69
28. S. Hinduja and M. Kunieda, *CIRP Annals – Manufact. Technol.*, 62 (2013) 775
29. J. Bannard, *J. Appl. Electrochem.*, 7 (1977) 1
30. B. Bhattacharyya, S. Mitra, A.K. Boro, *Robotics and Computer-Integrated Manufacturing*, 18 (2002) 283
31. D. Landolt, P.-F. Chauvy, O. Zinger, *Electrochimica Acta*, 48 (2003) 3185
32. P. Marcus, A. Teissier, J. Oudar, *Corrosion Science*, 24 (1984) 259
33. M. Łukaszewski, A. Czerwiński, *J. of Electroanalytical Chemistry*, 589 (2006) 38
34. R. Schuamacher, A. Müller, W. Stöckel, *J. of Electroanalytical Chemistry*, 219 (1987) 311
35. S. Zhou, M.M. Stack, R.C. Newman, *Corrosion Science*, 38 (1996) 1071
36. M.E. Folquer, S.B. Ribotta, S.G. Real, L.M. Gassa, *Corrosion*, 58 (2002) 240
37. Z. MácOvá, K. Bouzek, *J. of Applied Electrochemistry*, 42 (2012) 615
38. M. M. Lohrengel, C. Rosenkranz, Corrosion Sci., 47 (2005) 785
39. C. Rosenkranz, M.M. Lohrengel, J.W. Schultze, *Electrochimica Acta*, 50 (2005) 2009
40. M. M. Lohrengel, C. Rosenkranz, I. Klüppel, A. Moehring, H. Bettermann, B. Van den Bossche, J. Deconinck. *Electrochimica Acta*, 49 (2004) 2863
41. F. Andreatta, M.M. Lohrengel, H. Terryn, J.H.W. De Wit, *Electrochimica Acta*, 48 (2003) 3239
42. T. Haisch, E.J. Mittemeijer, J.W. Schultze, *Materials and Corrosion*, 53 (2002) 740
43. E. Lunarska, *Materials and Corrosion*, 47 (1996) 539
44. O. Weber, M. Weinmann, H. Natter, D. Bähre, *Journal Applied Electrochem.*, DOI 10.1007/s10800-015-0809-0
45. K. V. Subramaniam, M. Bi, *Corrosion Science*, 52(8) (2010) 2725
46. R. L. LeRoy, *Corrosion*, 31 (1975) 173
47. O. Weber O, H. Natter, A. Rebschläger, D. Bähre, Proceedings of the 7th International Symposium on Electrochemical Machining Technology, 5 (2011) 41
48. O. Weber, D. Bähre Proceedings of the 9th International Symposium on Electrochemical Machining Technology 7 (2013) 81
49. O. Weber, H. Natter, D. Bähre, *Journal of Solid State Electrochemistry*, DOI: 10.1007/s10008-014-2735-1
50. G.L. Song, A. Atrens, *Advanced Engineering Materials*, 1 (1999) 11
51. A. Popova, E. Sokolova, S. Raicheva, M. Christov, *Corrosion Science*, 45 (2002) 33

52. G. Song, A. Atrens, D. Stjohn, J. Nairn, Y. Li, *Corrosion Science*, 39 (1997) 855
53. K.P. Rataj, C. Hammer, B. Walther, M.M. Lohrengel, *Electrochimica Acta*, 90 (2013) 12
54. M.M. Lohrengel, S. Heiroth, K. Kluger, M. Pilaski, B. Walther, *Electrochimica Acta*, 51 (2006) 1431